Universiteit Utrecht

Bachelor thesis

Performance study of the FoCal detector sensors using cluster size data

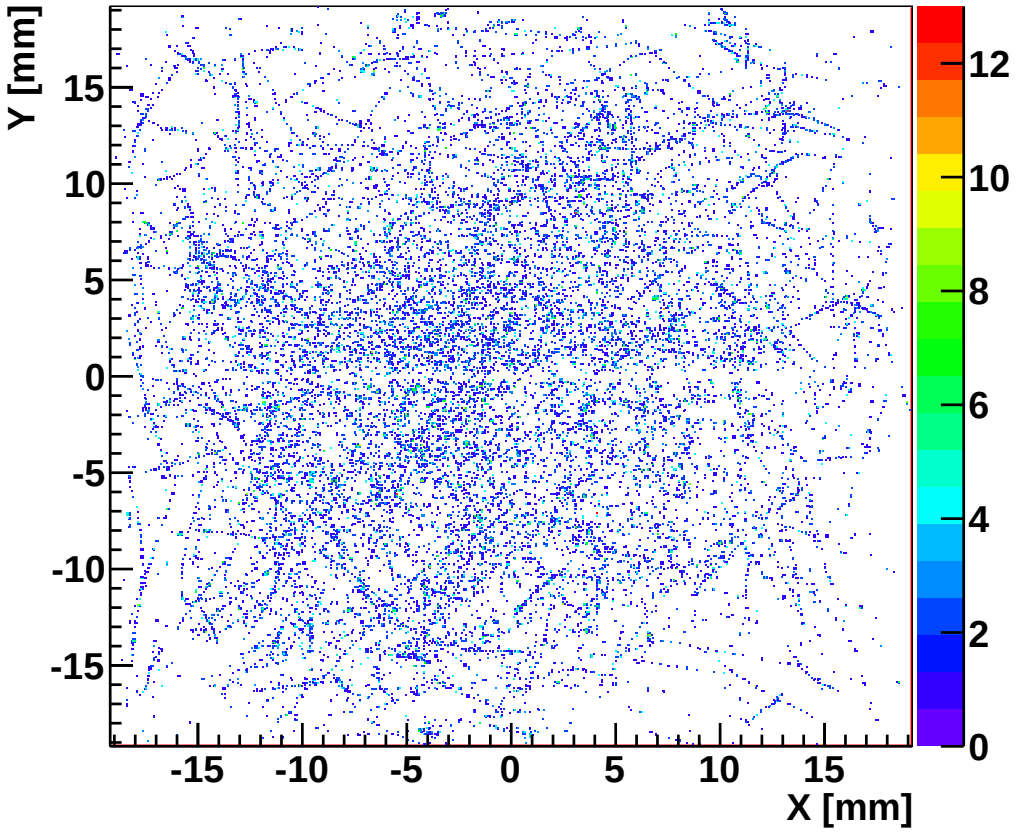

Author:
Monique Dorresteijn
Study: Physics & Astronomy
Student nr.: 3770184

Supervisor:
Marco van Leeuwen
Institute of Subatomic Physics
Daily supervisor:
Hongkai Wang
Institute of Subatomic Physics

Utrecht University
15 June 2016

Abstract

The FoCal is a proposed upgrade for the ALICE detector. The FoCal is an electromagnetic sampling calorimeter which uses digital pixel counting to measure the energy of the incoming particle. An important aspect of the detector response is the cluster size. In this thesis the goal was to examine if there is any external factor that can influence the cluster size. Factors investigated in this study are the incoming angle of the cosmic muons and the position of the cluster on the sensor. A simulation is performed to compare with the data and to see if the charge sharing model gives a realistic view of the observations. In the measured data no dependence between the cluster size and angle was found. Only when the angles in the simulation were larger than could be measured there was a dependence found. For the positional dependence the difference in the cluster size between the different channels was measured. Here there was no significant difference found.

Contents

Chapter 1

Introduction

In subatomic physics the building blocks of matter are studied. What are the elementary particles and how do they behave? For this there is a theoretical model called the Standard Model. The Standard Model describes for the behavior of elementary particles. In our every day life the electromagnetic and gravitational force are important. On subatomic length scales electromagnetism, the strong force and the weak force become more important. These forces describe the behavior of the subatomic particles, and how they interact.

To study these forces and particles at these small length scales, particle accelerators are constructed. The Large Hadron Collider (LHC) at CERN is one of those particle accelerators. Here lead ions and protons are collided. These collisions give information about the elementary particles and forces. ALICE (A Large Ion Collider Experiment) is one of the seven detectors which collect data from the LHC. The ALICE detector consists of a number of different sub systems, such as the Inner Tracking System, Time Projection Chamber and the Time of Flight detector. ALICE studies the quark gluon plasma (QGP), by measuring the energies of the particles coming out of the QGP produced in collisions of lead ions.

In this thesis, a prototype detector for ALICE is discussed, the Forward Calorimeter (FoCal). The FoCal is proposed as an upgrade for the ALICE detector. FoCal is a digital electromagnetic sampling calorimeter and will measure electromagnetic particles in the forward direction. In Figure 1.1 it can be seen where the FoCal detector will be placed in ALICE.

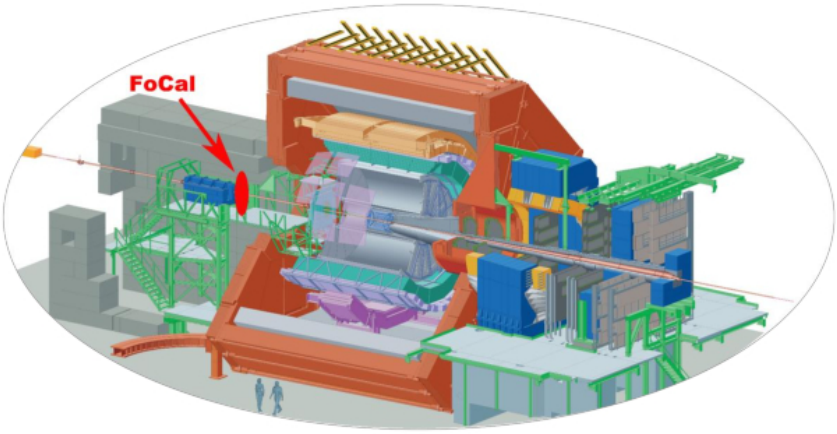

Figure 1.1 – The ALICE detector and the place where the FoCal would be placed.

At the moment the FoCal prototype is being tested by measuring cosmic muons. This is done to improve the analysis methods and discover the properties of the detector. The same setup is used in this thesis. The sensitivity of the detector is studied by investigating the size of clusters.

In the following chapter it will be explained why the FoCal detector is needed, furthermore information is given about cosmic rays, muons in particular. This is important, because the muons are used as test particles for the detector. Moreover general principles of particle detection

will be discussed. Afterwards the prototype will be thoroughly explained. Then the results of the experiment and simulations will be presented. Lastly the conclusion of the project will be presented.

For the analysis in this report 26335 cosmic muon tracks are used, more information about these runs can be found in Appendix A,

Chapter 2

Motivation

The motivation for building the FoCal prototype detector is:

- To demonstrate the feasibility of a pixel counting digital calorimeter
- To explore the possibilities offered by MAPS sensors in such an application
- To obtain detailed information on electromagnetic shower development in the scale of approximately 100 µm.

At the moment there is no good way to directly measure the energy of the π_0 particle. This particle has a 98.8% probability to decay into two photons. Measuring in the forward direction means the energy is high and the photons -due to conservation of momentum- travel in the same direction very close together after the collision. The resolution of the current detectors is not good enough to distinguish between the paths of these photons. At the moment there is no detector in the forward beam direction present at ALICE. With the FoCal the energy of charged particles with small angles with respect to the particle beam can be measured. This information is needed to further study the Quark Gluon Plasma (QGP).

To test the FoCal, a prototype is build and is being tested at Utrecht University. Beam tests have already been performed. In this bachelor thesis, data was used from the detection of cosmic muons. The sensor resolution was tested and whether it changes when the angle of incidence of the particles or the position of the particles changes.

Chapter 3

Cosmic rays

3.1 Hadronic showers

When a cosmic ray hits the atmosphere a shower of particles is created. A combination of Bremsstrahlung and pair production causes this cascade of particles, also called a hadronic shower. As Figure 3.1 shows, the shower consists of protons, neutrons, kaons, pions, photons, electrons and positrons. Most of the particles decay before they can reach the earth's surface. Most pions will decay into muons according to the following interaction:

$$\pi^- \longrightarrow \mu^- + \overline{\nu}_\mu \tag{3.1}$$

Figure 3.1 also shows the muons reach the earth's surface. Muons are unstable and will eventually decay into an electron and two neutrinos.

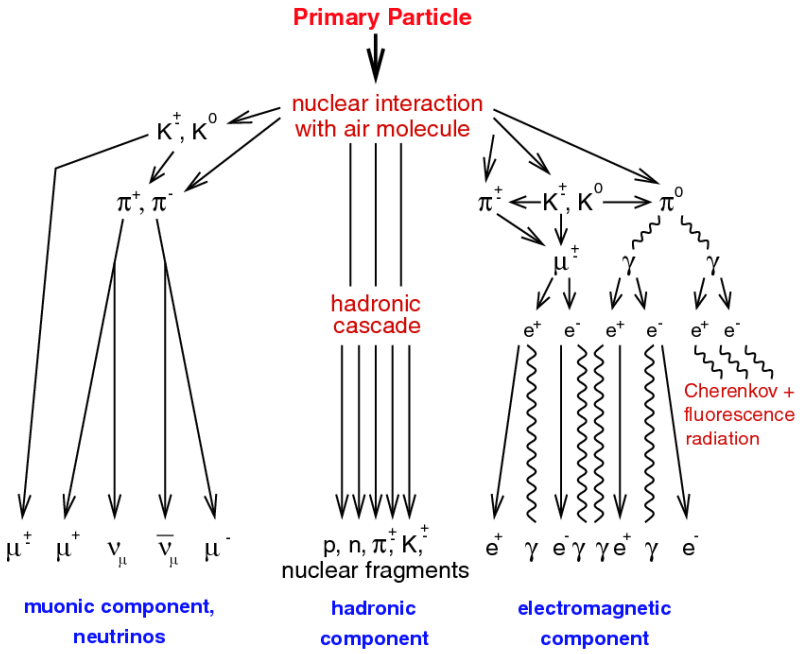

Figure 3.1 – A cosmic shower with the three main components separated (Enqvist [2009]). On the left side, muons are presented.

3.2 Muons

Muons are elementary particles which are part of a group called leptons. There are two kinds of muons: positively charged and negatively charged (anti-muon). The rest mass of the muon is $m_\mu = 105.66$ MeV/c^2.

Muons are the most numerous charged particles at sea level (Olive and Particle Data Group [2014]). These muons are created high above the earth's surface in the cosmic showers. The lifetime of a muon is $\tau = 2.197$ µs (Grieder [2001]). The muons reach the surface due to their speed and the relativistic effects caused by this speed.

The energy of the muons is dependent on the travel distance. The distance is dependent on the zenith angle thus the energy is also dependent on the zenith angle. The detector used can only measure small angles, therefore an average energy is assumed. The average energy of the muons at sea level is $E_\mu = 4$ GeV. At higher or lower energies, the flux of muons is significantly lower.

The amount of muons that reach sea level is the flux. This flux can be calculated by Equation 3.2 in [cm^{-2}s^{-1}] (Grieder [2001]). For the downward flux we need to integrate the intensity across the solid angle from the zenith in all directions.

$$J = I(\theta)\cos\theta \, \mathrm{d}\Omega \tag{3.2}$$

where $I(\theta)$ is given by:

$$I(\theta) = I_v \cos^2(\theta) \tag{3.3}$$

where $I_v = 0.0083$ cm^{-2}s^{-1}sr^{-1} and θ is the zenith angle (Rossi [1948]). To calculate the flux as a function of the zenith angle we integrate over the solid angle. The flux does not depent on the azimuthal angle (Schultheiss [2016]).

$$\begin{aligned} J(\theta) &\approx 2\pi \int_0^\theta \left(I_v \cos^2\theta\right) \cos\theta \sin\theta \, \mathrm{d}\theta \\ &\approx \left(\frac{\pi}{2}\right) I_v \left(1 - \cos^4\theta\right) \end{aligned} \tag{3.4}$$

This gives us the flux of the muons per area.

Chapter 4

Particle detection

A calorimeter is designed to measure the energy of particles. It exploits the fact that the particles interact via the electromagnetic interaction. The electromagnetic interaction produces a shower of electrons. The electrons then interact with the sensor material, which in turn can be measured. By interacting with the material, the particle loses energy by depositing it on the detector. By adding all the energy depositions of the shower the energy of the incoming particle can be calculated.

There are two types of calorimeters, homogeneous and sampling. A homogeneous calorimeter only consists of sensor material. This calorimeter has a very high resolution, but also has some drawbacks. For example the calorimeter needs to be very large to contain the energy of the particle.

Sampling calorimeters consist of absorber and sensor layers. The absorber is a heavy material that makes sure the particles produce a shower. The sensor then measures the energy deposition of the shower. Downside of this way of measuring is that the energy deposited on the non sensitive areas of the detector is not measured. This means that the total energy of the shower needs to be estimated.

Material dependent scaling constants tell us how particle detectors needs to be designed to contain enough energy of the shower, so the energy of the incoming particle can be calculated. These scaling constants give the relation between the shower and the detector material. The scaling constants are the radiation length and the Molière radius.

4.1 Radiation length

The radiation length X_0, is defined as the distance in a material in which a high energy electron (or positron) will lose on average 63.2% of its energy. A particle detector needs to be many radiation lengths long to measure the energy of the incoming particles. The radiation length is given by the following equation 4.1:

$$X = X_0 \frac{\ln(E_0/\epsilon_c)}{\ln(2)} \tag{4.1}$$

Here ϵ_c is the critical energy with an estimated value of: $\epsilon_c = 610\text{MeV}/(\text{Z} + 1.24)$ (Olive and Particle Data Group [2014]). Here Z is the atomic number of the material in which the shower takes place. The atomic number of the material is an important factor for the radiation length.

4.2 Molière radius

The Molière radius tells us how wide the particle shower becomes. This is dependent on the material in which this shower takes place. The Molière radius is given by:

$$R_M = E_s \frac{X_0}{\epsilon_c} \tag{4.2}$$

where E_s is the scale factor: $E_s = \text{m}_e\text{c}^2\sqrt{4\pi/\alpha}$. Approximately 95% of the shower is contained laterally in a cylinder with radius $2R_\text{M}$. A smaller Molière radius leads to a better shower resolution.

4.3 Muon detection

Muons mainly lose their energy through ionization (Olive and Particle Data Group [2014]). The energy loss is given by the Bethe-Bloch equation (Equation 4.3).

$$\frac{\mathrm{d}E}{\mathrm{d}x} = -2\pi N_a r_e^2 m_e c^2 \rho \frac{Z}{A}\frac{z^2}{\beta^2}\left[\ln\left(\frac{2m_e\gamma^2 v^2 W_{max}}{I^2}\right) - 2\beta^2\right] \tag{4.3}$$

Here, N_a is Avogadros constant, r_e the electron radius, m_e the electron rest mass and ρ the density of the material. The factors β and γ are the relativity factors. W_{max} gives the maximal transferable energy, I is the average excitation energy, z is the charge of the incoming particle. The fact that the energy loss is almost independent of the energy for large energies makes the muons an ideal candidate to use for the calibration of calorimeters.

Chapter 5

Experimental setup

The experimental setup, as used in this thesis, is presented in Figure 5.1, the red box shows the actual detector. The detector is constructed of layers of sensors and absorber material, forming a tower of 936 mm high. The seperate parts of the detector are explained in the following sections.

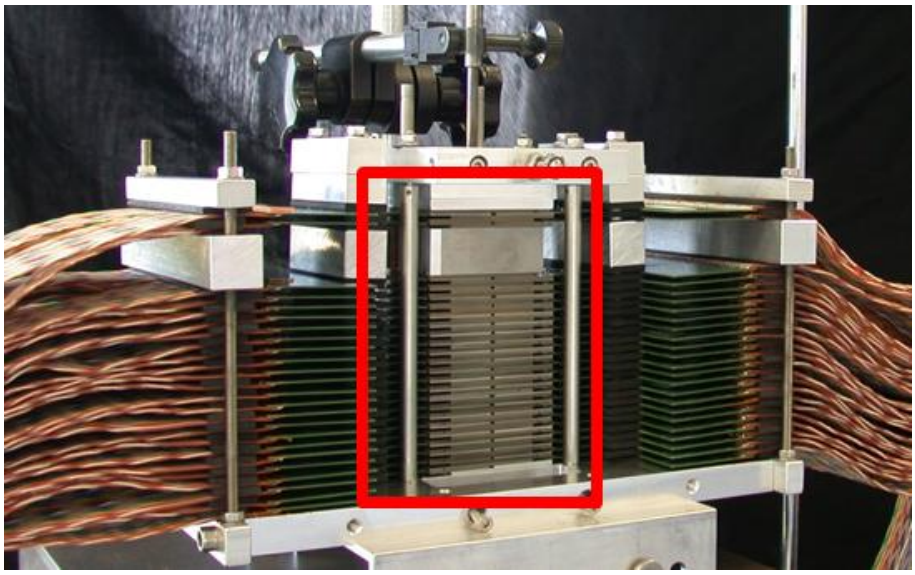

Figure 5.1 – A picture of the setup as it was used in this experiment. The red box highlights the sensors and absorbers layered on top of each other.

5.1 Scintillators

In the setup two scintillators are connected. One above and one below the detector. If both scintillators give a signal at the same time, the detector readout is sent to the computer (this is called a trigger). This ensures that there is not a lot of useless data. A downside of measuring this way is that there is a maximum angle that can be measured. The maximum angle depends on the surface area and the distance between the two scintillators. This zenith angle is $\theta = 13.2$ degrees for this setup.

When a charged particle travels through the scintillator, a photon is emitted. The photon is redirected to the photo-multiplier tube, where a cascade of electrons is made. The photo-multiplier tube does this to amplify the signal so it can be measured. The scintillators have a transverse size of 40 by 40 mm^2 and are mounted such that the sensitive region of the calorimeter is covered.

5.2 Layers

In between the scintillators are 24 layers of detection material and 24 layers of tungsten absorber. The total thickness of a single layer is 4 mm, of which 3 mm consists of tungsten (W). The detection layer consists of four sensors placed as seen in Figure 5.2. Every chip is set in a certain quadrant and numbered as in the figure. The absorption layers are made of tungsten because this material

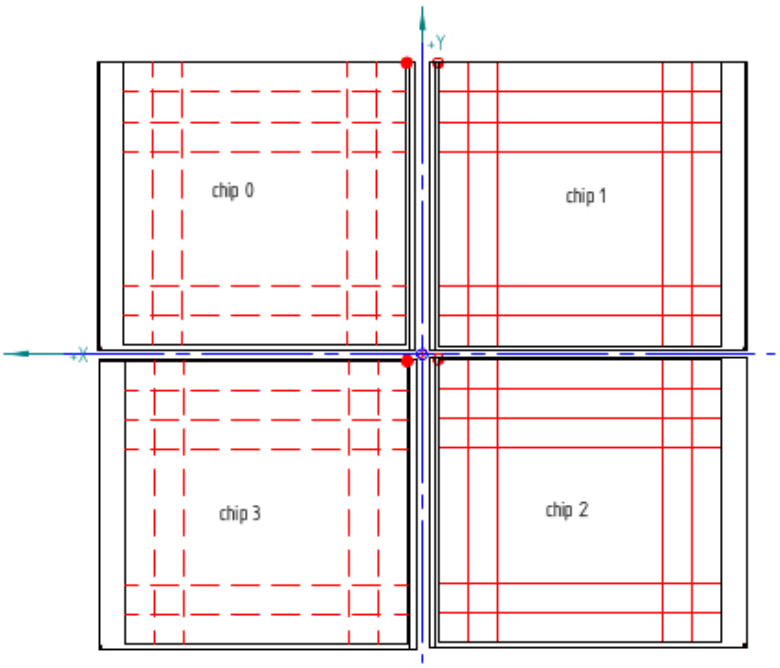

Figure 5.2 – The way the sensors are placed in every layer of the detector.

has a very small Molière radius (0.9 cm). Every layer is made out of a lot of different parts. The contribution of the various materials to the Molière radius is given in Table 5.1. The way the

Table 5.1 – Layer information. Adjusted table from Reicher [2016]

Material	X_0 [cm]	R_M [cm]	Thickness [mm]
W	0.35	0.9	3.38
Air	30390	7330	0.23
Si	9	4.9	0.12
G10	19	7.5	0.102
Cu	1.4	1.6	0.058
Epoxy	33	8.4	0.04
Ag	1.2	1	0.04
Total layer	0.97	1.07	3.97

sensors are put together is shown in Figure 5.3. A module is made from two sensors mounted on the tungsten absorber. There is a small gap between the sensors but this is unavoidable. The modules in every layer are placed as presented in Figure 5.4. Here A is the sensor, B the electronics and C the tungsten absorber. The modules overlap a little bit.

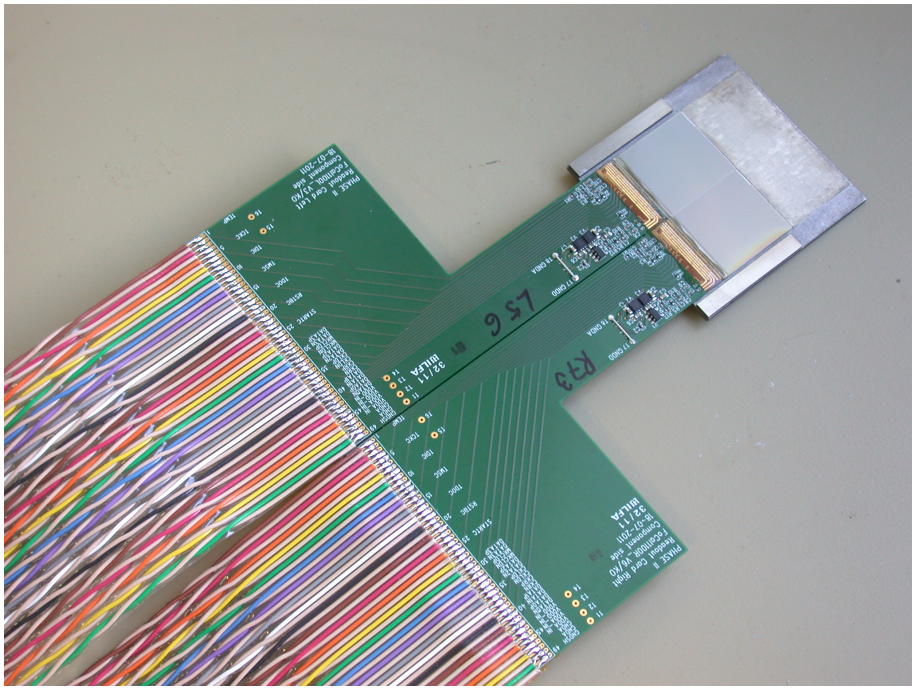

Figure 5.3 – The sensor mounted on the tungsten absorber and the printed circuit board.

5.3 Sensor

The FoCal prototype uses PHASE-II Mimosa23 sensors. These sensors are designed by the Institut Pluridisciplinaire Hubert Curien in Strasbourg. These kinds of silicon detectors are called: Monolithic Active Pixel Sensors (MAPS). The sensors are made of a silicon semiconductor.

This silicon has different doping levels built up in layers within the sensor. Levels are shown in Figure 5.5, they are the $p++$, $p+$ and p-epitaxial layer. The charge produced by the cosmic muon moving through the layer is collected in the n-well. The charge flows through the layers by diffusion. When the charge reaches the n-well the pixel is activated.

These sensors allow continuous readout of all pixels. The size of the active part of the sensor is 19.2mm by 19.2mm. In the detector there are three types of sensors present. These sensors differ in thickness of active silicon namely: 14 µm, 15 µm and 20 µm. Each sensor has 640 lines and 640 columns, which leads to 409600 pixels with a 30 µm pitch. The sensor readout is done by a rolling shutter system, this means the readout is line by line. When the line is read, the signal of each pixel is sent to the discriminator at the end of each column. The readout of a sensor is called a frame. This readout method is not yet fast enough for high energy physics, but causes no problems in our test measurements.

Each chip has two adjustable parameters VREF1 and VREF2. The first regulates the threshold of the detection and the other is the sensitivity uniformity along the chip.

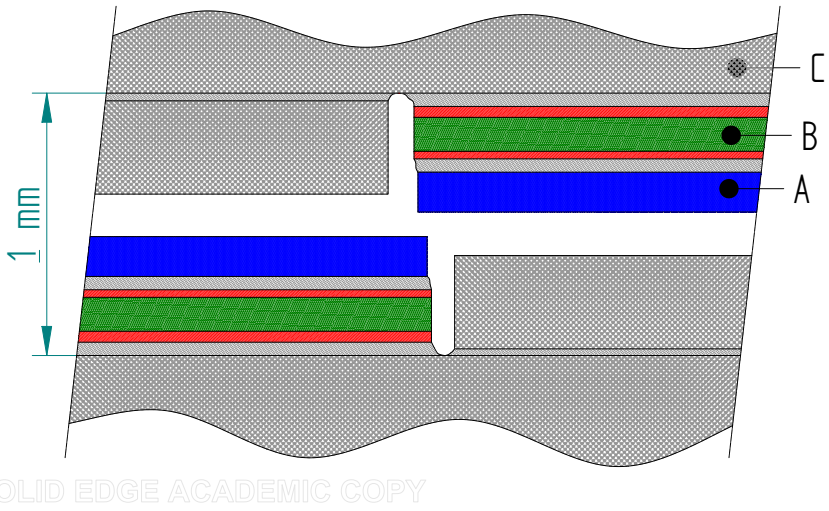

Figure 5.4 – Schematic of tungsten and sensor. A is the sensor, B the printed circuit board and C the tungsten absorber.

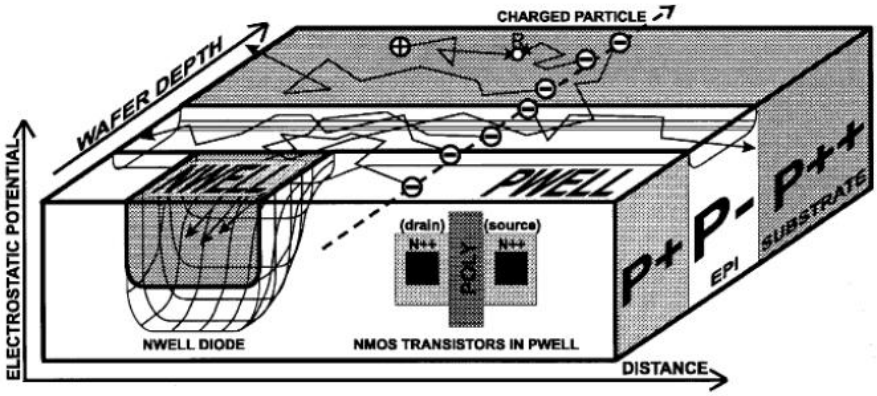

Figure 5.5 – The sensor schematic with different doping levels.

5.4 Data acquisition

Figure 5.6 shows a schematic of the data readout process of the sensors. Each chip has 4 channels, 160 columns per channel. Each sensor chip performs two steps of multiplexing before sending the data to 4 output channels to be read out at 160 MHz. The signals are then combined by the Spartan6 FPGA (Field Programmable Gate Array). The output of two Spartan FPGAs is read by one Virtex6 FPGA. Two Virtex FPGAs are needed to read out all sensors and send the data to the DAQ computer. The raw data on the computer then needs to be de-multiplexed and analyzed. A pedestal run is taken to take out the noise from the data. The FoCalDAQ system contains the software to start and stop measurements. This system is also used to set the chip parameters.

In the Cosmic readout all data are continuously written to the buffer of the Bergen boxes and the read-out of this buffer is trigger driven. Data belonging to a trigger is shipped to the FoCalDAQ computer when the buffer is full.

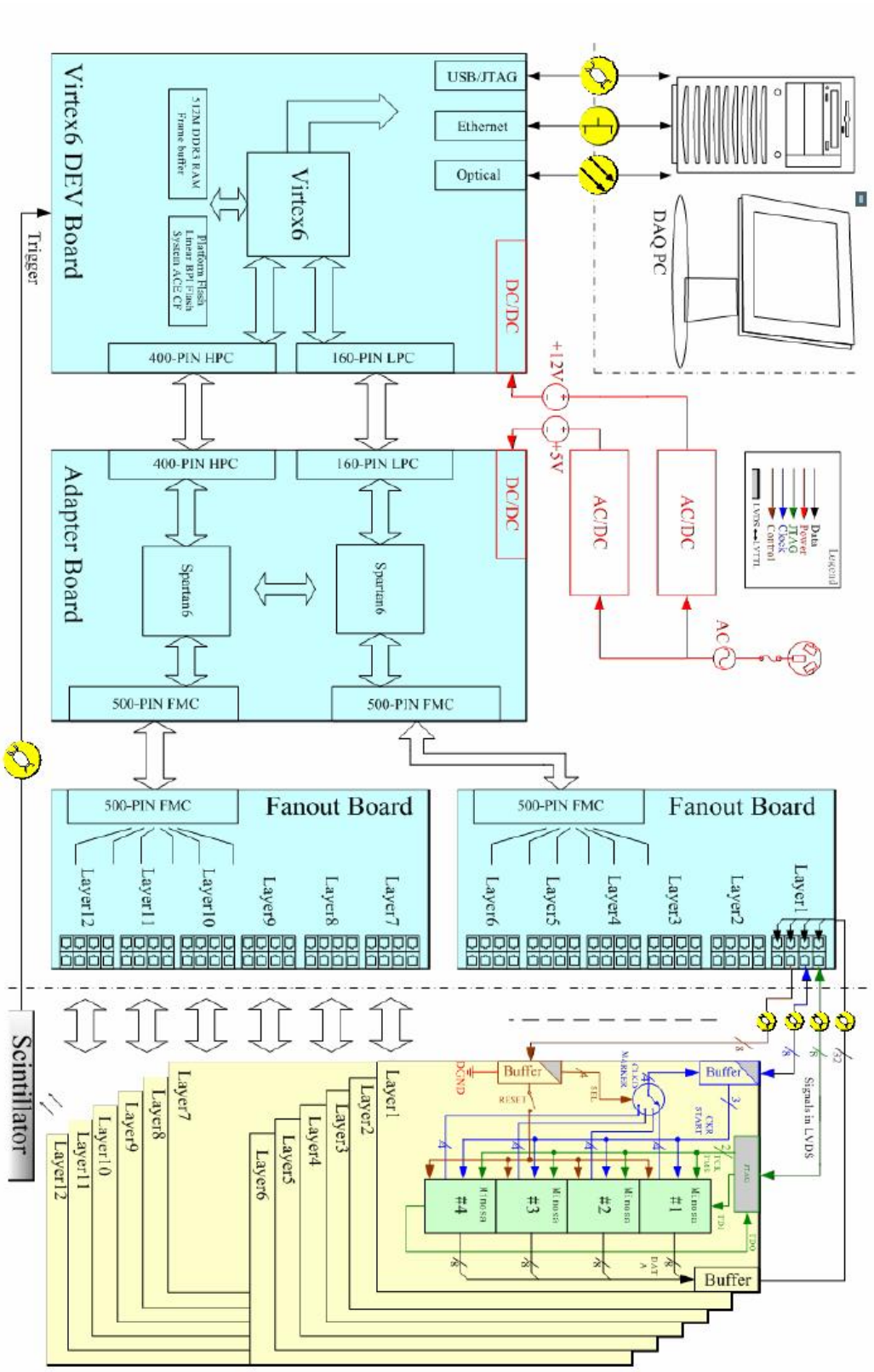

Figure 5.6 – The scheme shows how the data is sent from the sensors to the computer.

Chapter 6

Data analysis

In this chapter the data analysis process is explained. The hitmap is a 2D representation of the detector from above. This data is digital which means each pixel is either 1 or 0. Where the 1 means a particle is detected and a 0 means that no particle is detected. Some effects can change the value of the pixel, sometimes there is a hit but no particle went through (noise) or there is no hit but a particle went through. This occurs when the particle leaves no energy deposit on the sensor. By decreasing the threshold, more particles can be detected but there will also be more noise. Increasing the threshold lowers the sensor sensitivity.

In Figure 6.1 there are 741 muon tracks displayed. A white band around $Y = 0$ is visible. This is not due to data loss but because the sensors are a few hundred micron apart. In the other direction, the sensors overlap slightly which gives more hits on the hitmap but this is not seen in this figure because not enough data is displayed.

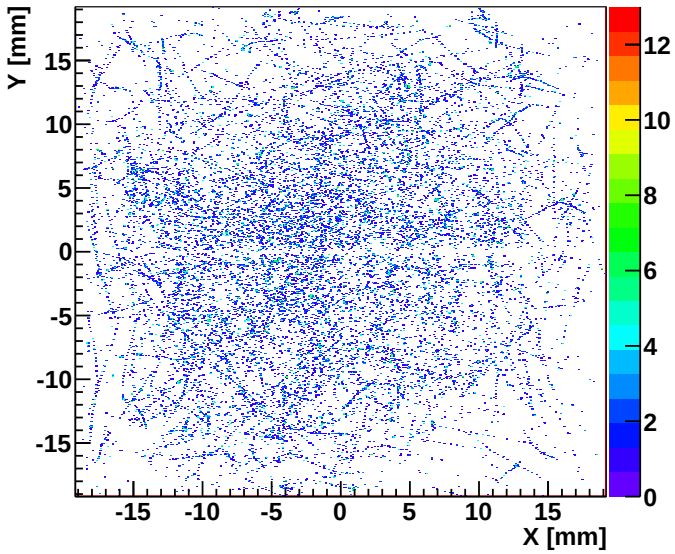

Figure 6.1 – All the hits from all the sensors, data from run 967. The times a pixel is activated is given by the colour.

6.1 Tracker

Cosmic rays were used for testing the FoCal prototype. The cosmic ray mostly consist of muons. It is assumed that the muons do not interact with the tungsten layers. However, sometimes the muons do interact with the tungsten layer, this effect is corrected in the analysis. The muons go in a straight line through the detector. The track procedure makes a straight line through the hits, this is shown in Figure 6.2. The only thing that can change is the zenith and azimuthal angle at

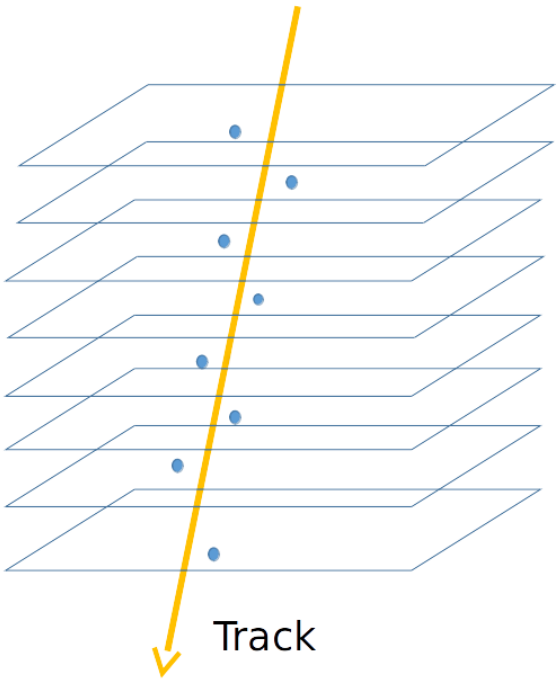

Figure 6.2 – A schematic view of how the track is being calculated from the hits.

which the muon goes through the detector. The procedure for making tracks from the hits is as follows (Reicher [2016]):

- Combine hits into tracklets
- Find a region of interest
- Use the tracklet with the highest number of neighboring tracklets as seed for a proto-track
- Assign all hits that are closer than 1 mm to the seed line to the proto-track
- If the photo-track has at least 24 hits assigned to it in at least 12 layer, promote it to a full track
- Repeat the process until no further tracks can be created.

6.2 Angle

The tracker fits a straight line through the hits. From this straight line, the zenith angle can be calculated using:

$$\tan\theta = \frac{\sqrt{\triangle\ Y^2 + \triangle\ X^2}}{\triangle\ Z} \tag{6.1}$$

Here the $\triangle\ X$ and $\triangle\ Y$ values are the displacement of the track in the plane of the sensors and $\triangle\ Z$ is the length of the detector.

6.3 Clusters

A cluster is a group of hits, belonging to a single particle. While muons traveling through the detector are so small they only go through one pixel. The muon ionizes the silicon, and the charge that is produced by this process can diffuse to another pixel. This process of charge diffusion produces clusters. With a threshold noise level of 10^{-5}, about 2 to 4 pixels are activated when a muon travels through the sensor. These clusters are typically square shaped.

Chapter 7

Measurement results

7.1 Expectation

The goal of this thesis is to investigate the dependence of the cluster size on the angle of the incidence of particles and on the location of the hits within the sensor. First the angles in which the particles enter the detector is reviewed. The expectation is that there will be larger clusters at larger angles. This is due to the charge sharing as is explained in Section 6.3. There is no directional preference, thus the clusters should on average be square. This can be tested by calculating the cluster size in a certain direction. The clusters are sensor dependent, so differences between sensors also have to be verified. As seen in Appendix B there is a lot of difference between the sensors apart from just the different size of the active layer.

It is important to know if there is any angle dependence because this could affect the results when measuring cascades of high energy particles. It also is a fact that is useful to know in general.

7.2 Angle dependence

The cluster sizes are distributed as shown in Figure 7.1. Here it becomes clear the clusters vary in size but most of them are 5 pixels or less.

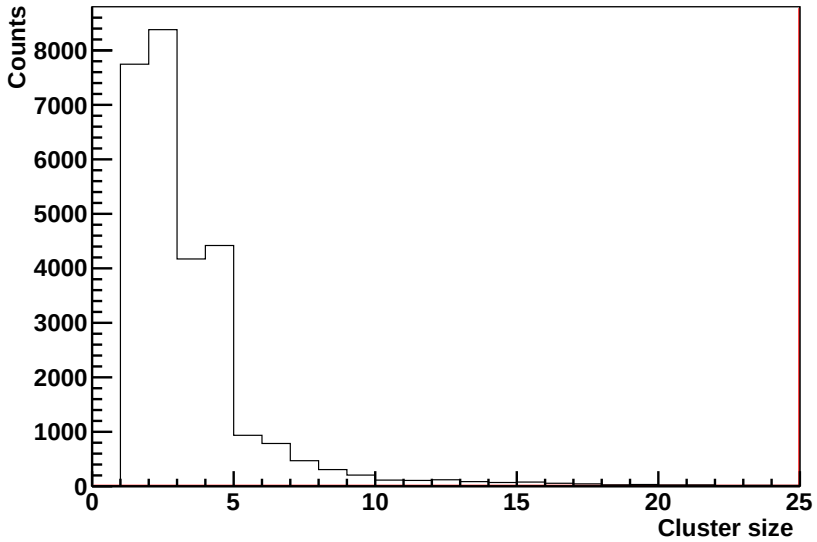

Figure 7.1 – Cluster size distribution

Figure 7.2 shows there is no dependence on the angle as mentioned in Section 7.1. The black line is the average cluster size per angle and is a near perfect horizontal line, so no dependence is visible. Rise in the cluster size at angles larger than 15 degrees is visible, but there are also a lot of smaller clusters. This is not surprising as there are no angles possible beyond 13.2 degrees. Larger angles could be measured due to the effect that the muons interact with the tungsten absorber, hereby changing direction. The measured particles could also be other particles than muons, such as for example other cosmic particles. The tracker assumes the muons move in a straight line. The average cluster size here is 3.46 ± 0.39 pixels. At the larger angles then 15 degrees there is just not enough data to give an average with certainty. If the angles that cannot be measured because of the scintillators are left out, an average of $3,45 \pm 0,12$ pixels is found. The dependence of the cluster size in the X and Y direction on the angle in the XZ and YZ plane

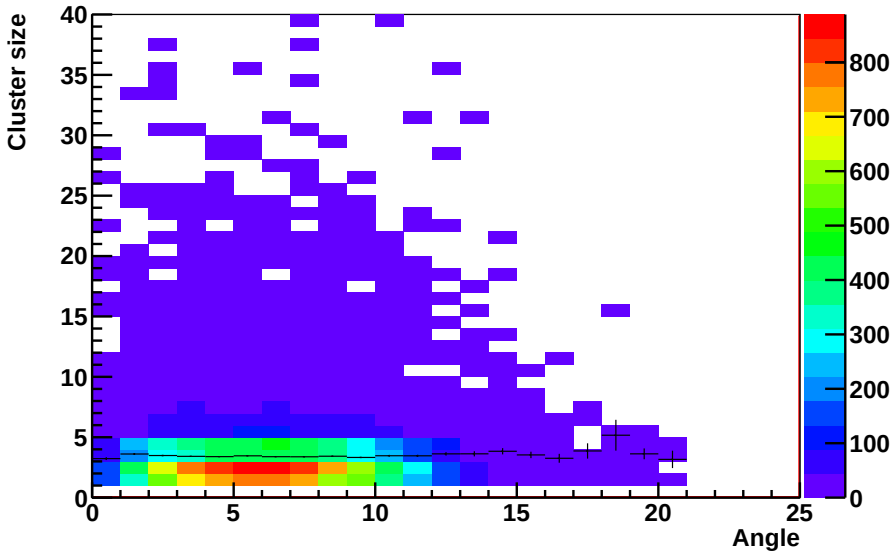

Figure 7.2 – The cluster size dependence on the zenith angle, here the black line is the average cluster size per angle.

respectively, where investigated separately. Unfortunately, lots of problems occur when there is a directional preference, this indicates problems in the hardware or software. Since there is no preferred direction in which particles reach the detector. As seen from figure 7.3a and figure 7.3b there is no directional preference observed. The averages of the different directions is 1.86 ± 0.15 pixels for the X-direction and 1.87 ± 0.05 pixels for the Y-direction. Since the values are near identical we see that the clusters are mostly square shaped.

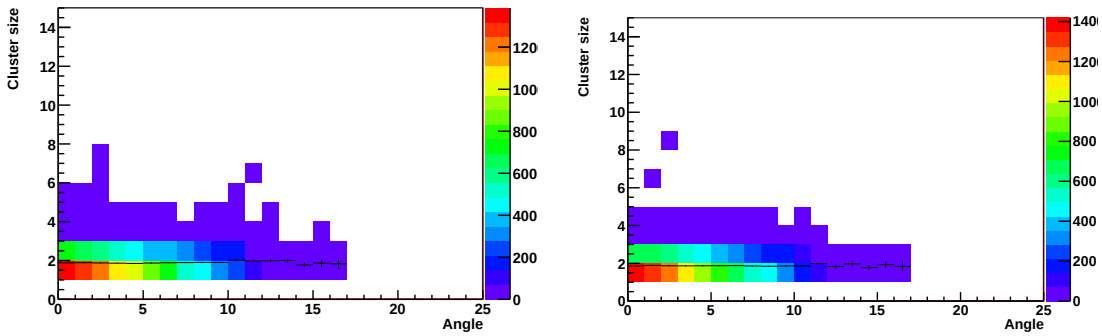

(a) X direction **(b)** Y direction

Figure 7.3 – The cluster sizes in the different directions

7.3 Position dependence

If the cluster size changes between different positions, the difference is most likely found between the channels. The channels are horizontal bars in the sensor, they are numbered from the center of the detector outward as presented in Figure 7.4. The channels have a separate data collection and response is explained in Section 5.4 this makes them ideal candidates to examine for a positional dependence. The difference between the channels can be seen from the hitmaps of the sensors in Appendix B. Even if three of the four channels work perfectly, the last can be fully or partially broken. The Vref2 value that influences the left-right balance of the sensor can be set to a not optimal setting, which means there could be a difference in the cluster size.

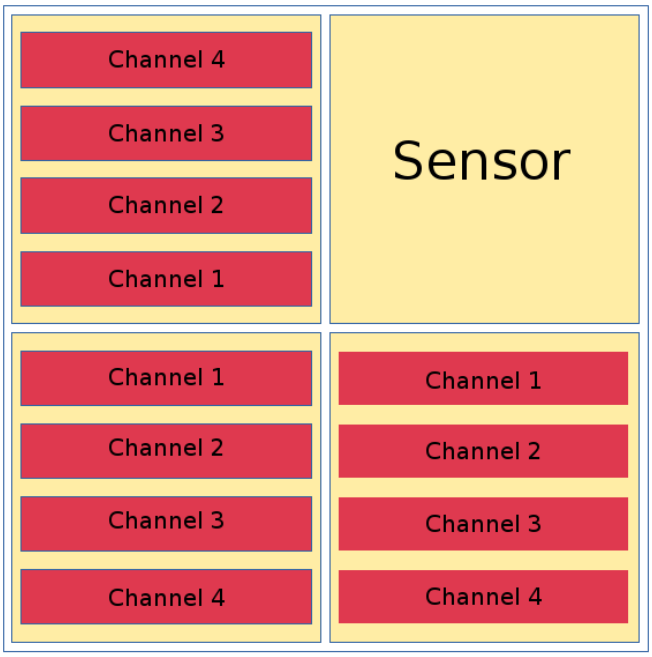

Figure 7.4 – Channels as numbered in the analysis.

From Figure 7.5 it is clear that there is not a lot of difference in average cluster size between the channels. This effect is overall seen on all the sensors.

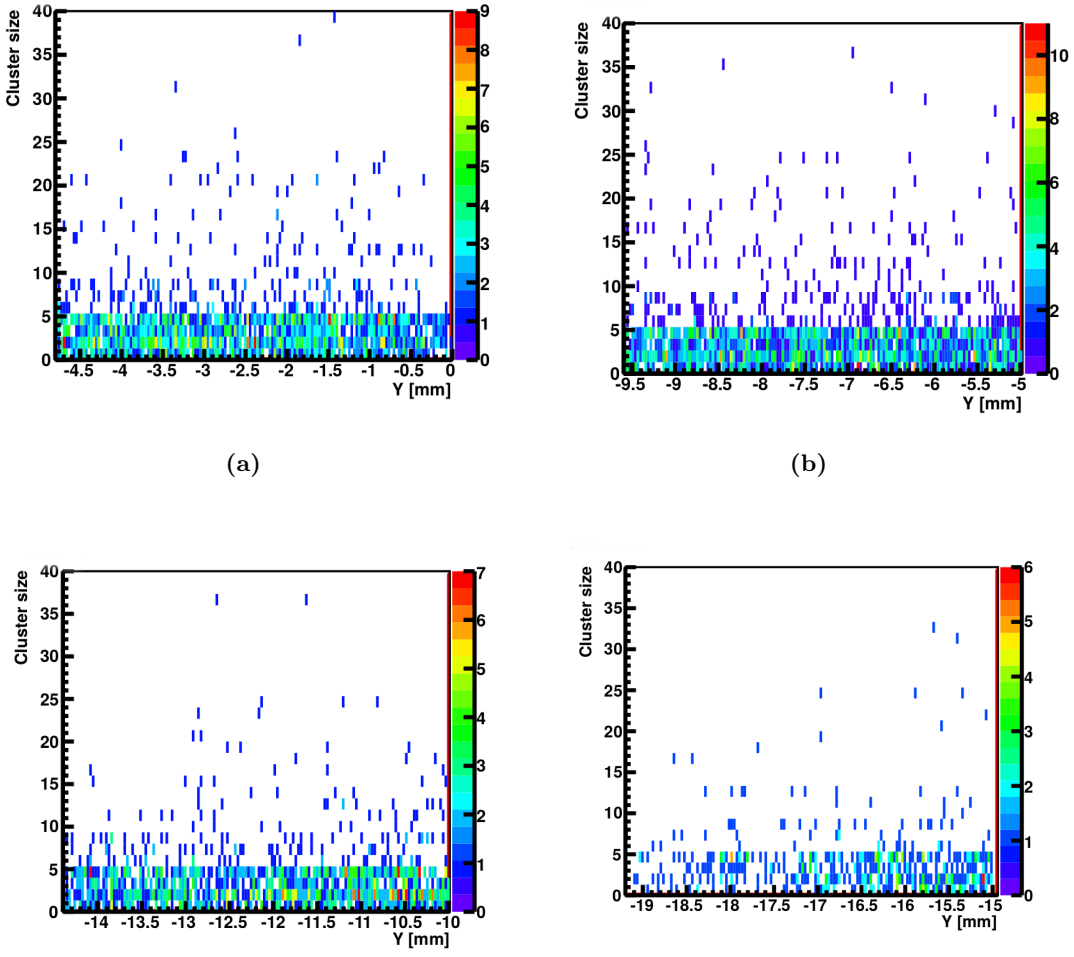

Figure 7.5 – The different channels of sensor 61. Where 7.5a is channel 1, 7.5b is channel 2, 7.5c is channel 3 and 7.5d is channel 4.

The problem with examining the difference in cluster size between the channels is the amount of data is different per channel. This difference is due to the effect that most particles are collected in the center of the detector. The channel in a sensor furthest from the center has typically four times fewer hits than the channel nearest to the center of the detector as seen in Table 7.1.

Table 7.1 – The cluster sizes of the different channels for sensor 61.

Channel	# of Tracks	Average cluster size [pixels]
1	1691	3.52 ± 0.08
2	2256	3.55 ± 0.09
3	1422	3.48 ± 0.09
4	474	3.7 ± 0.2

Figure 7.6 presents the difference between the channel closest to the detector center (1) and channel 3. The last channel does not have enough data to make an accurate comparison. Sensors: 24, 25, 33, 51, 64 and 76 gave no signal. The orange values have a large uncertainty, these are the sensors: 17, 26, 27, 30, 41, 65 and 85. Apart from sensor 30 all of them have a broken channel or are only partially working which explains the large uncertainty. The green values have a significant difference in cluster size between the two channels, these are the sensors: 8, 34, 38, 43, 45, 50, 53, 57, 63, 72, 75 and 78. Of only three of these sensors could be explained why there is a significant difference between the channels. For the other sensors no explanation can be given on why there is a significant difference. In Appendix B the hitmaps of all the sensors are given, these hitmaps show if the channels are working properly.

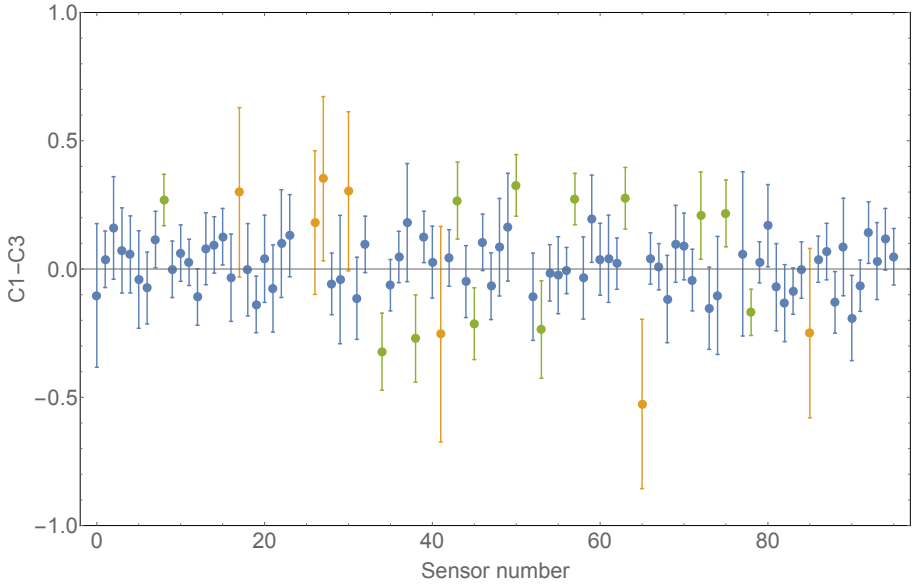

Figure 7.6 – The difference between the channels closest to the detector center and the third closest channel. Here the orange points have the largest uncertainties and the green points have a significant difference in cluster size between the two channels.

Chapter 8

Simulation

Geant3 is used for the simulation of the detector and the particles sent through them. The simulation uses Monte Carlo methods to simulate the particles that propagate through the detector and the interactions with the detector material. The full prototype is simulated without the imperfections of the sensors.

To make a comparison to the data taken from FoCal, the angular distribution of the muons is simulated with the azimuthal angle set to an uniform distribution. The average energy of the muons is set to 4 GeV, this is comparable to the average energy of muons at sea level. In this thesis there was no noise simulated.

The response of the sensor pixel is simulated by the sharing model. The muon passing through the pixel creates a charge. This charge then diffuses outward as is presented in Figure 8.1. The charge sharing model gives a realistic view of how many pixels would be activated when a muon goes through.

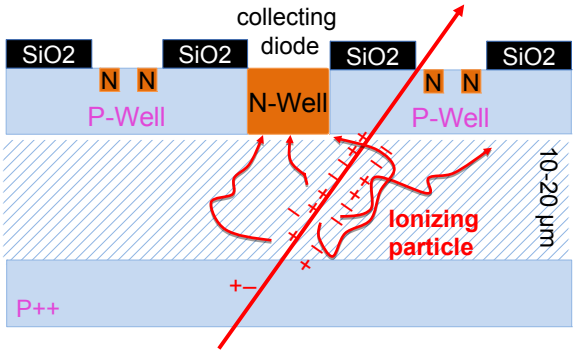

Figure 8.1 – A schematic view of the charge sharing model.

8.1 Results

As seen from figure 8.2, the cluster size distribution of the simulation looks similar to the experimental data. With a large difference in the amount of clusters with size one. The average cluster size for the simulation is 3.34 ± 0.16 pixels. This is similar to the value we found for the measurements of $3,45 \pm 0,12$ pixels in Section 7.2.

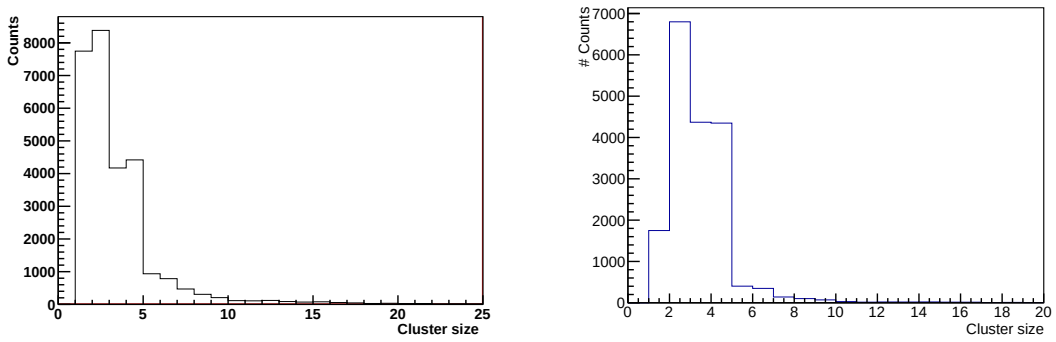

(a) **(b)**

Figure 8.2 – In figure 8.2a the cluster size distribution from the FoCal measurements and in 8.2b the simulated cluster size distribution.

Figure 8.3 shows the cluster size dependence on the angle for the same angle range as observed. The figure also shows angles larger than 13.2 degrees, it is unknown how these angles can occur in the simulation. An other observation is the angles at which there is data is smaller than found in the prototype. In the measured data there are no clusters at angles larger than 21 degrees while in the simulation the angles stop at 17 degrees, no explanation can be found for this difference.

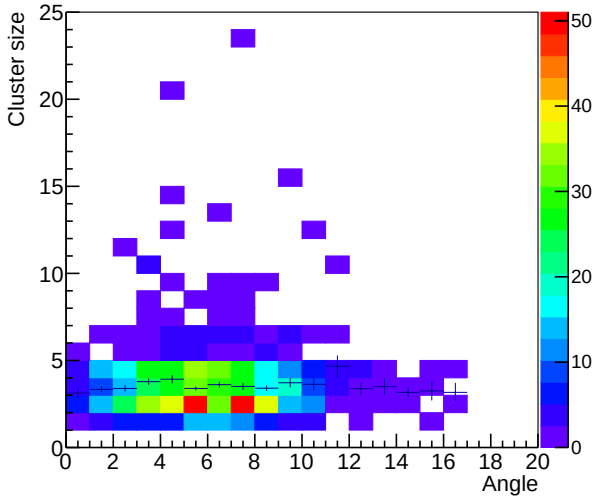

Figure 8.3 – The cluster size dependence on the zenith angle, with simulated data.

In the FoCal prototype it is not possible to make large angles, since the muons have to go through both scintillators to be measured. In the analysis of the simulated data, the tracker is not used. So the track does not have to go through all the layers. For the simulated data, the muons only needed to go through the first three layers in the detector. Because this was the only restriction set on the angles, large angles could be achieved. Due to this angles of 65 degrees are possible, which is useful for the analysis of the showers. In the simulation a uniform distribution of the angles is used, thereby in contrast to the prototype data, this gives us enough statistics to say something about the large angles. This in turn gives us smaller uncertainties.

As seen in Figure 8.4 and Figure 8.5 the cluster size increases with increasing angles, but this effect starts at angles larger than 30 degrees. At smaller angles as seen from the prototype data there is no effect found. This can be explained by calculating the path length of the muons through a sensor.

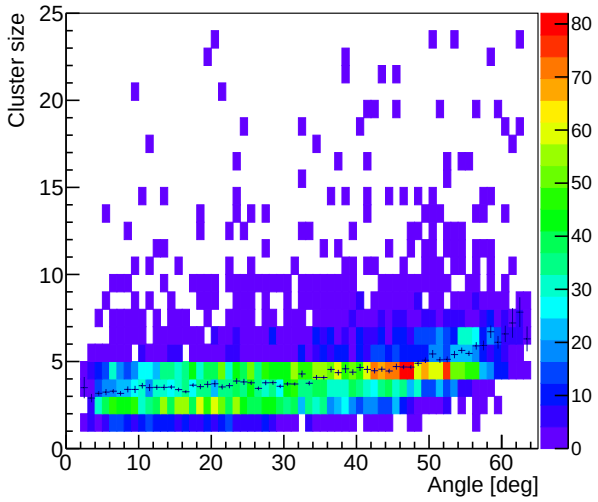

Figure 8.4 – The cluster size dependence on the zenith angle, from simulated data.

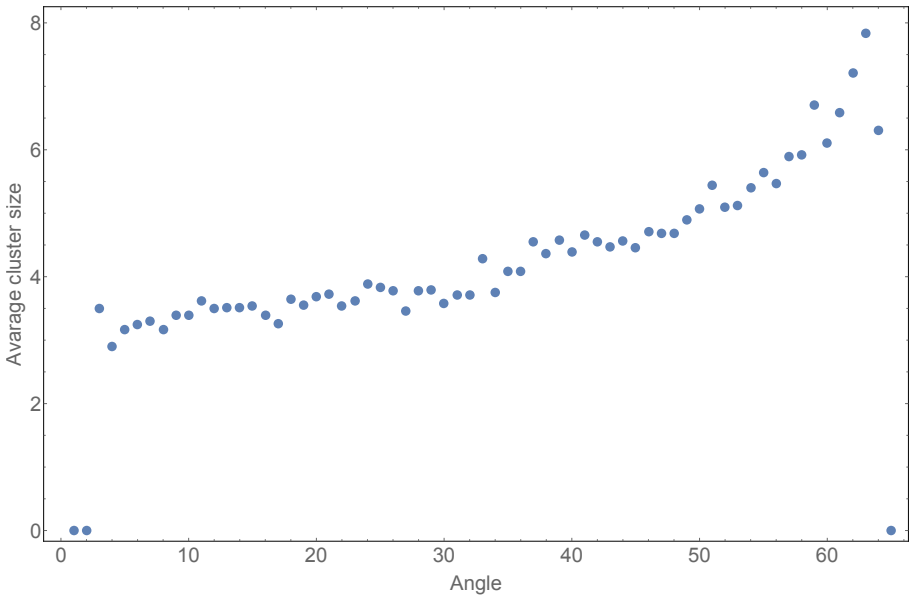

Figure 8.5 – The average cluster size as a function of the zenith angle from simulated data.

Chapter 9

Conclusion

The goal of this thesis was to find if there is any external factor that can influence the cluster size. Factors that were researched are the incoming angle of the cosmic muons and the position. Here was found that there is a dependence, but this is only found in the simulations. The angles needed to see an effect are much larger than the FoCal prototype can measure. The effect of larger cluster sizes has to do with the path length of the muons in the sensor layer.

The position dependence is also examined but here more research is needed. There is a lot of difference between the sensors in sensitivity and average cluster size. Within the sensors there is hardly any difference in cluster size found. A problem that occured during this study was that some sensors are broken or are only partially working.

It is found that the simulation of the charge sharing of the pixels is simulated in a way that mimics the reality. The data of the detector and the simulation is similar. The biggest difference was in the amount of clusters with size one. The charge sharing model needs some adjustment to compensate for this effect.

Appendix A

Cosmic runs

Table A.1 – Runs used for this experiment

Run	Tracks	Details
967	741	
968	2751	
969	1102	
970	1159	
971	846	
972	1000	
973	1190	
974	1087	
975	1469	
976	0	Pedestal run
977	1368	
978	1199	
979	722	
980	1896	
981	1157	
982	1765	
983	1765	
984	676	
985	2437	
986	1135	
987	1798	
Total	26335	

Appendix B

Sensors

On the next four pages the sensor hitmaps are displayed. The number of the sensor is shown in the corner and the layer number is given below.

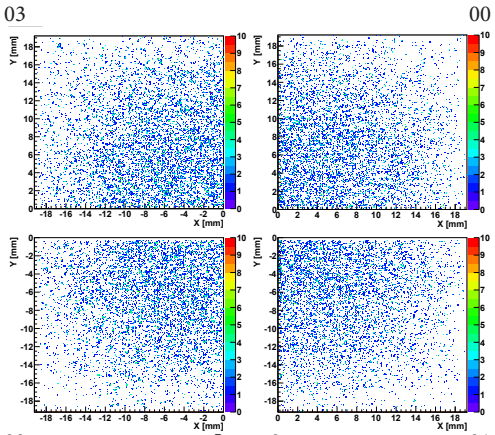
03
00
02
Layer 0
01

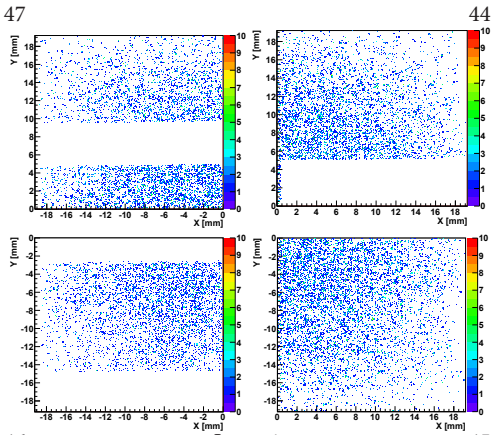
47
44
46
Layer 1
45

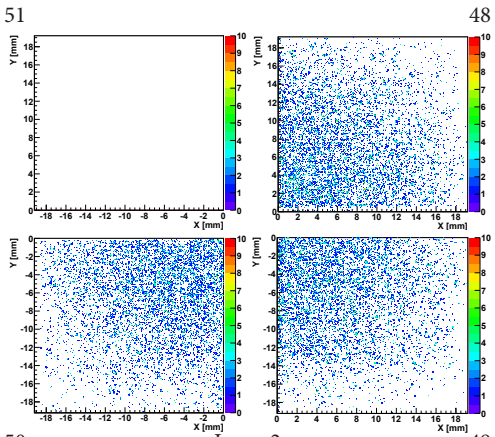
51
48
50
Layer 2
49

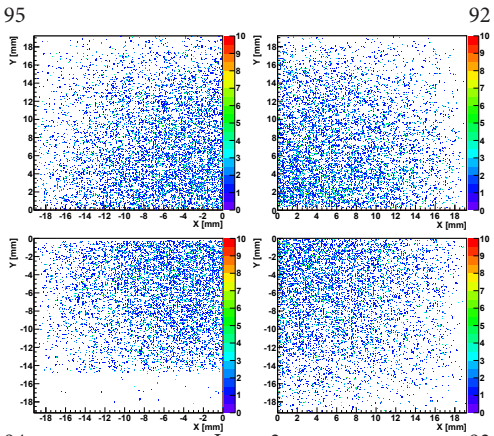
95
92
94
Layer 3
93

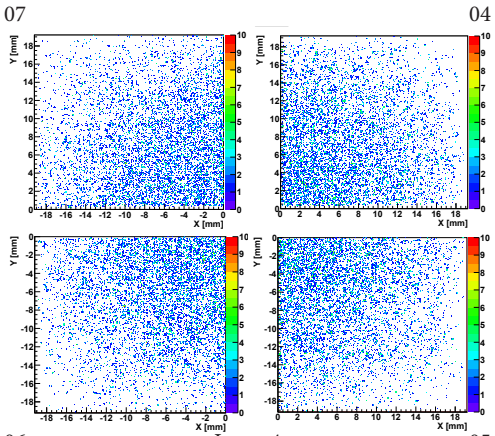
07
04
06
Layer 4
05

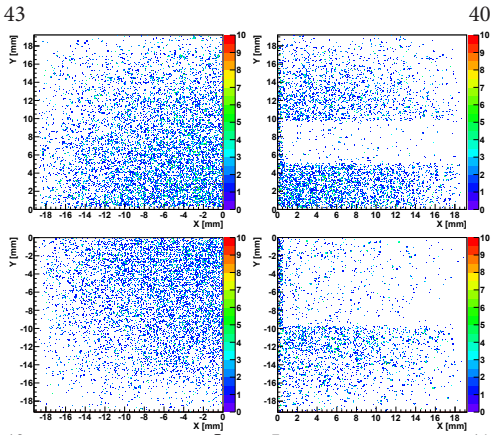
43
40
42
Layer 5
41

55 52

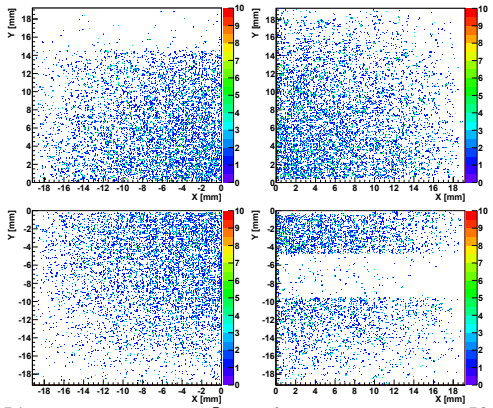

54 Layer 6 53

91 88

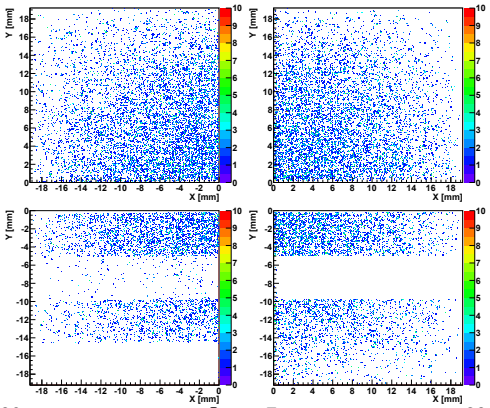

90 Layer 7 89

11 08

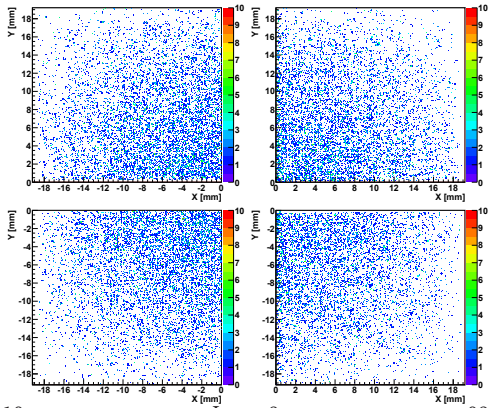

10 Layer 8 09

39 36

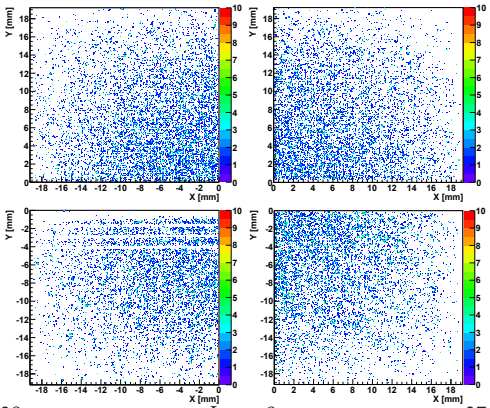

38 Layer 9 37

59 56

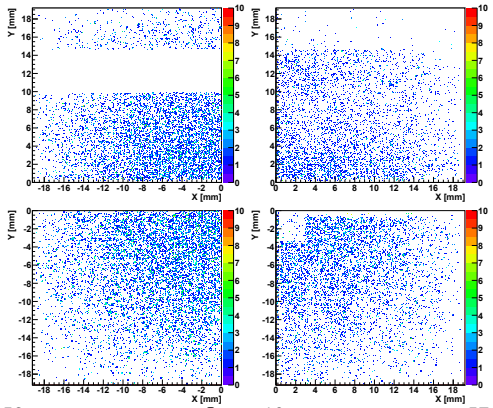

58 Layer 10 57

87 84

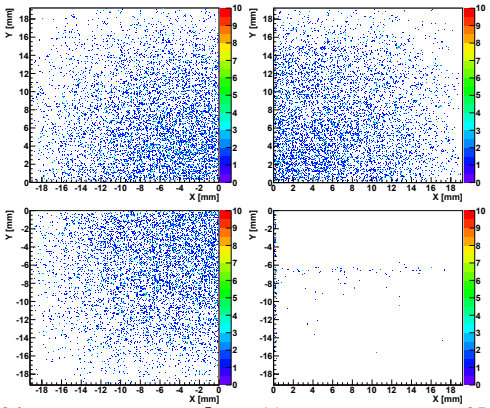

86 Layer 11 85

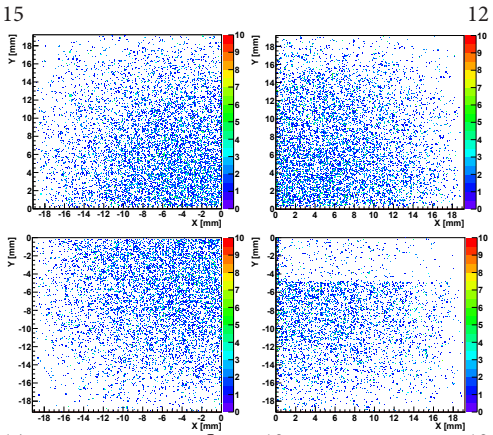
15
12
14
13
Layer 12

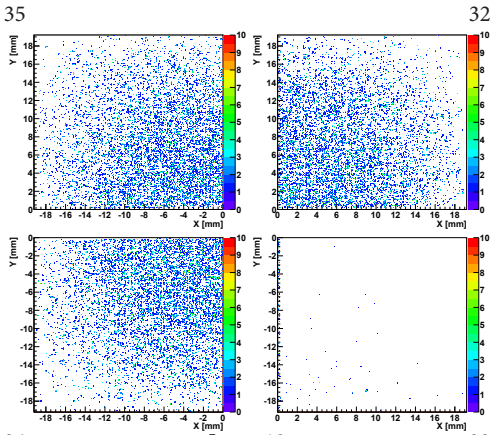
35
32
34
33
Layer 13

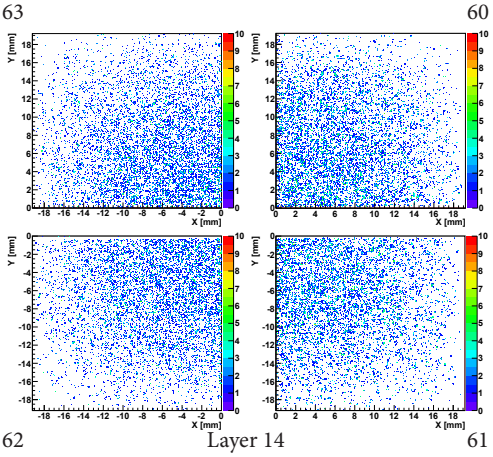
63
60
62
61
Layer 14

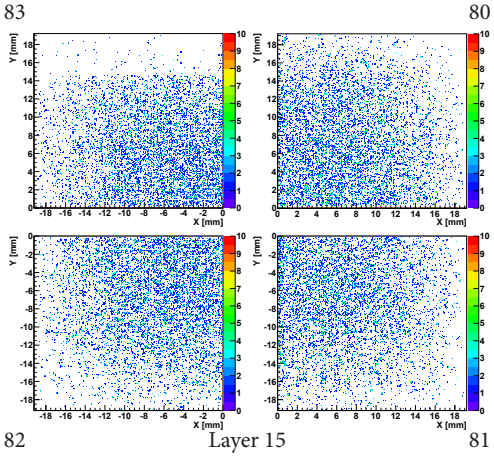
83
80
82
81
Layer 15

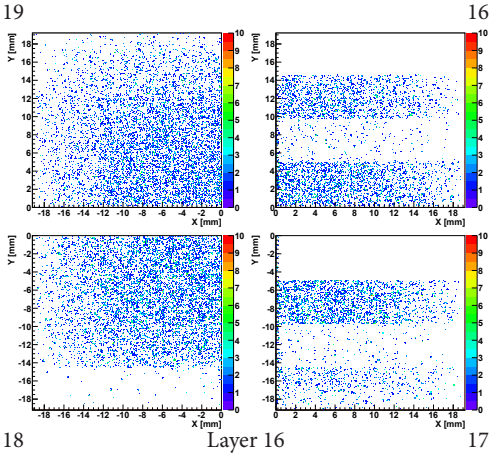
19
16
18
17
Layer 16

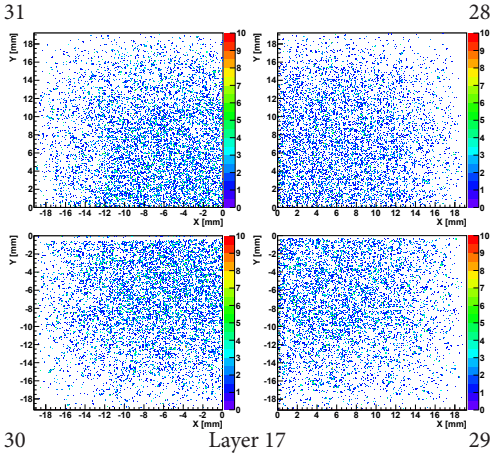
31
28
30
29
Layer 17

67 64

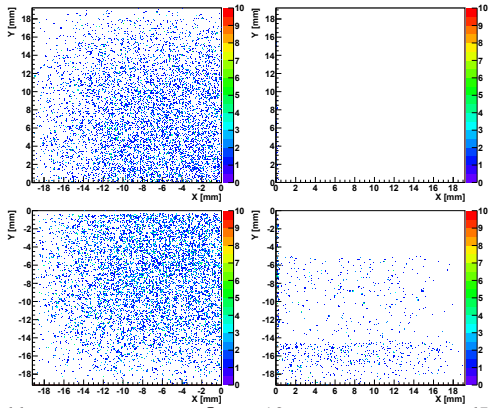

66 Layer 18 65

79 76

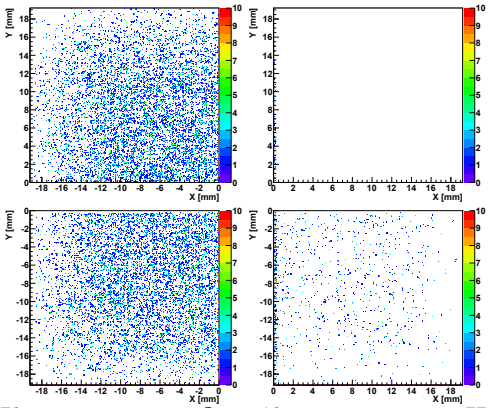

78 Layer 19 77

23 20

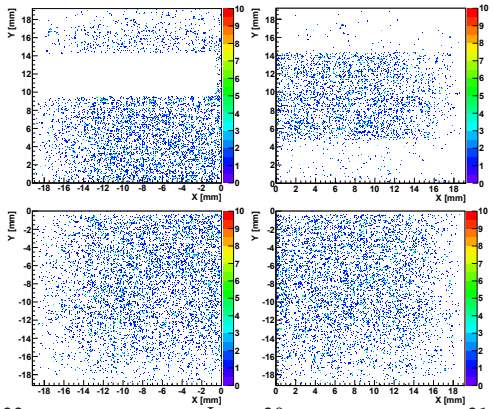

22 Layer 20 21

27 24

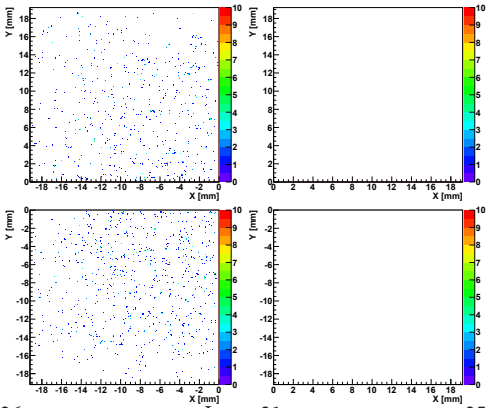

26 Layer 21 25

71 68

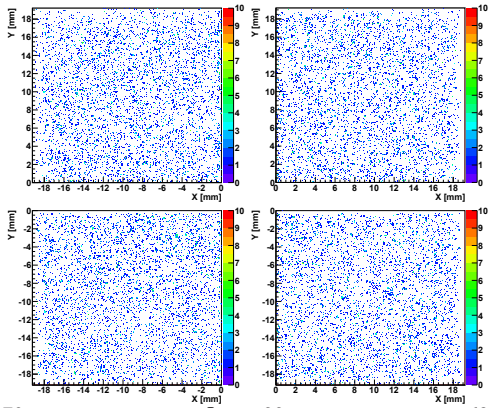

70 Layer 22 69

75 72

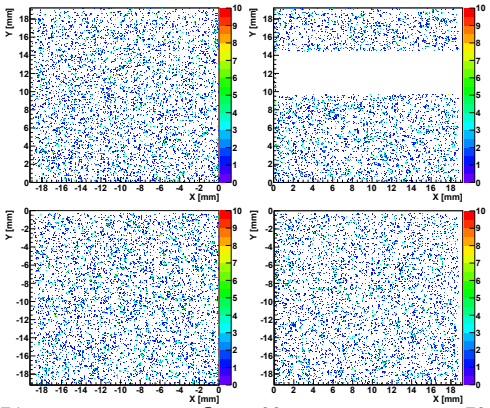

74 Layer 23 73

Bibliography

Enqvist, T. (2009). Astroparticle physics lecture notes. University of Oulu. cupp.oulu.fi/timo/opetus/lecture-app2009-1.pdf.

Grieder, P. K. (2001). *Cosmic rays at Earth*. Gulf Professional Publishing.

Olive, K. A. and Particle Data Group (2014). Review of particle physics. *Chinese Physics C*, 38(9):090001.

Reicher, M. (2016). Digital calorimetry using pixel sensors.

Rossi, B. (1948). Interpretation of cosmic-ray phenomena. *Rev. Mod. Phys.*, 20:537–583.

Schultheiss, N. (2016). The field of view of a scintillator pair for cosmic rays. *arXiv preprint arXiv:1601.00849*.

Acknowledgements

I would like to thank a few people for helping me on this project. Fist of all I need to thank Marco for guiding me through the project. Gert-Jan for answering all my questions and asking me questions. Thomas for his explanation about the detector and its purpose. The of course I need to thank Hongkai for answering my questions daily and his help in understanding the FoCal programs. Chungui for letting me use his simulation program and Figure 8.1. Daan also needs to be thanked for helping with some of the ROOT programming.

For the grammar and spelling I had some help of my roommates Jennifer and Elsa. Where Elsa even spent a evening making sensor hitmaps look nice. Swinda was a great help with her knowledge of physics and how a thesis should look. The thesis would have been a dramatic mess if it was not made beautiful by the LaTeXcode of Laurens.

The last persons that need to be thanked are Selma and Niels for our mutual encouragement to finish this thesis successfully.